A proposed crystal structure of delamanid, $C_{25}H_{25}F_3N_4O_6$

Tawnee M. Ens[1], James Kaduk[1,2], Megan Rost[3], Anja Dosen[3] and Tom Blanton[3]
[1]*Department of Physics, North Central College, 131 South Loomis Street, Naperville, IL 60540, USA*
[2]*Department of Chemistry, Illinois Institute of Technology, 3101 South Dearborn Street, Chicago, IL 60616, USA*
[3]*International Centre for Diffraction Data (ICDD), 12 Campus Boulevard, Newtown Square, PA 19073-3273, USA*

(Received 12 November 2024; revised 12 May 2025; accepted 18 May 2025)

Abstract: The crystal structure of delamanid has been solved and refined using synchrotron X-ray powder diffraction data and optimized using density functional theory techniques. Solution and refinement of the structure presented significant difficulties, and the result should be considered proposed or approximate. Delamanid crystallizes in the space group $P2_12_12_1$ (#19) with a = 67.3701 (18), b = 12.86400(9), c = 5.65187(12) Å, V = 4,898.19(14) Å^3, and Z = 8 at 295 K. There are two independent delamanid molecules, with different conformations, which are essentially identical in energy. The crystal structure consists of layers of delamanid molecules perpendicular to the a-axis. The imidazooxazole ring systems stack along the b-axis, and the trifluoromethyl groups make up the boundaries of the corrugated layers. There are no classical hydrogen bonds in the crystal structure. Eight C–H···O and one C–H···N hydrogen bonds contribute to the lattice energy. The powder pattern has been submitted to the International Centre for Diffraction Data for inclusion in the Powder Diffraction File™ (PDF®).
© *The Author(s), 2025. Published by Cambridge University Press on behalf of International Centre for Diffraction Data. This is an Open Access article, distributed under the terms of the Creative Commons Attribution licence (http://creativecommons.org/licenses/by/4.0), which permits unrestricted re-use, distribution and reproduction, provided the original article is properly cited.* [doi:10.1017/S0885715625100845]

Key words: delamanid, Deltyba, crystal structure, Rietveld refinement, density functional theory

I. INTRODUCTION

Delamanid (marketed under the trade name Deltyba) is administered to treat tuberculosis and is used in combination therapy as a first line of defense against multidrug resistance. Delamanid works by being activated by a bacterial enzyme in the nitroreductase class, with the intermediate molecule being involved in blocking the production of mycolic acids, which help bacteria avoid the immune system and antibiotic treatment (Gler et al., 2012; Xavier and Lakshmanan, 2014; Zhao et al., 2015). Delamanid is European Medicines Agency (EMA)-approved, and although not extensively FDA-approved, it is allowed for use in multidrug-resistant cases (Lardizabal et al., 2017; Mudde et al., 2022). This drug shows promising results from the limited currently published international studies, acting more rapidly and having greater potency against tuberculosis than some other treatment options (Xavier and Lakshmanan, 2014; Pontali et al., 2019). The systematic name (CAS Registry No. 681492-22-8) is (2R)-2-methyl-6-nitro-2-[[4-[4-[4-(trifluoromethoxy) phenoxy]piperidin-1-yl]phenoxy]methyl]-3H-imidazo[2,1-b] [1,3]oxazole. A two-dimensional molecular diagram of delamanid is shown in Figure 1.

Commercial Deltyba is formulated as an amorphous solid dispersion with poly(hydroxypropyl methylcellulose phthalate) (Duong et al., 2022). In an attempt to increase the solubility of delamanid, Duong et al. prepared several sulfonate salts and also reported a powder diffraction pattern of crystalline delamanid. The EMA (2013) indicates that the enantiomeric purity of delamanid is routinely controlled by chiral high performance liquid chromatography (HPLC) and that no polymorphs or solvates have been found.

This work was carried out as part of a project (Kaduk et al., 2014) to determine the crystal structures of large-volume commercial pharmaceuticals and include high-quality powder diffraction data for them in the Powder Diffraction File™ (Kabekkodu et al., 2024).

II. EXPERIMENTAL

Delamanid was a commercial reagent, purchased from Achemblock (Batch #18775) and was used as received. The light beige powder was packed into a 1.5-mm-diameter Kapton capillary and rotated during the measurement at ~50 Hz. The powder pattern was measured at 295 K at beamline 11-BM (Antao et al., 2008; Lee et al., 2008; Wang et al., 2008) of the Advanced Photon Source at Argonne National Laboratory using a wavelength of 0.458133(2) Å from 0.5 to 50° 2θ with a step size of 0.001° and a counting time of 0.1 seconds per step. The high-resolution powder diffraction data were collected using 12 silicon crystal analyzers that allow for high angular resolution, high precision, and accurate peak positions. A mixture of silicon (NIST SRM 640c) and alumina (NIST SRM 676a) standards (ratio Al_2O_3:Si = 2:1 by weight) was used to calibrate the instrument and refine the monochromatic wavelength used in the experiment.

Corresponding author: James Kaduk; Email: kaduk@polycrystallography.com

https://doi.org/10.1017/S0885715625100845 Published online by Cambridge University Press

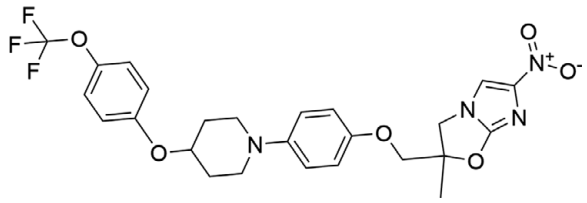

Figure 1. The two-dimensional structure of delamanid.

The pattern was indexed using DICVOL14 (Louër and Boultif, 2014) on a primitive orthorhombic unit cell having a = 67.50965, b = 10.35692, c = 6.43550 Å, and V = 4,499.65 Å^3. The unit cell volume is consistent with Z = 8. A reduced cell search of the Cambridge Structural Database (Groom et al., 2016) yielded three hits, but no delamanid derivatives.

Establishing the space group was difficult. Several space group interpretation routines suggested the extinction symbol *Pb_b*, especially preferring *Pbnb* (Z' = 1). The glide planes are inconsistent with pure *R*-delamanid. The highest-ranked proper space group was $P2_12_12_1$, which would require Z' = 2. The structure was thus solved and refined in both *Pbnb* and $P2_12_12_1$. The centrosymmetric space group (P*bnb*) yielded $R_{wp} \sim 20.4\%$, while the non-centrosymmetric space group ($P2_12_12_1$) yielded $R_{wp} \sim 17.8\%$ (with about twice as many parameters). To confirm the absence of a center of symmetry, a second harmonic test was carried out (Figure 2). The SHG is a quadratic function of the laser power level, so the sample is non-centrosymmetric, and thus the suggested space group was $P2_12_12_1$.

The delamanid molecular structure was downloaded from PubChem (Kim et al., 2023) as Conformer3D_CID_6480466.sdf. It was converted to a *.mol2 file using Mercury (Macrae et al., 2020). The crystal structure was solved using Monte Carlo-simulated annealing techniques as implemented in EXPO2014 (Altomare et al., 2013), using two *R*-delamanid molecules as fragments, with a bump penalty and [100] preferred orientation.

Rietveld refinement (starting from the VASP-optimized structure) was carried out with GSAS-II (Toby and Von Dreele, 2013). Only the 0.7–22.0° portion of the pattern was

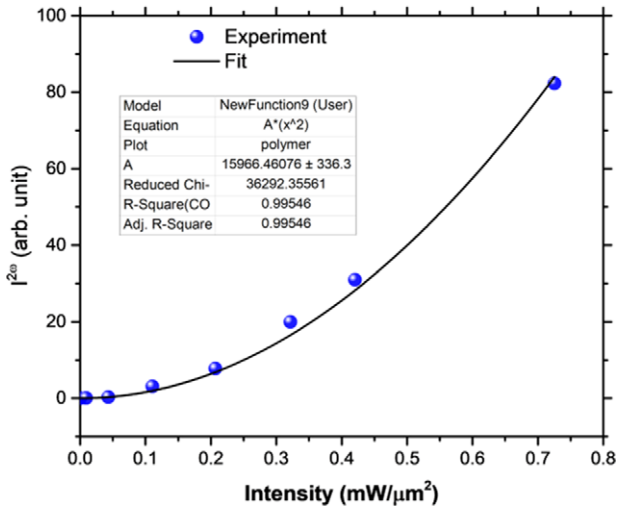

Figure 2. Second harmonic generation test results for delamanid, confirming the absence of a center of symmetry.

included in the refinements (d_{min} = 1.200 Å). All non-H-bond distances and angles were subjected to restraints, based on a Mercury/Mogul Geometry Check (Bruno et al., 2004; Sykes et al., 2011). The Mogul average and standard deviation for each quantity were used as the restraint parameters. The phenyl rings and the fused ring systems were restrained to be planar. The restraints contributed 15.1% to the final χ^2. The hydrogen atoms were included in calculated positions, which were recalculated during the refinement using Materials Studio (Dassault Systèmes, 2023). The U_{iso} of the heavy atoms were grouped by chemical similarity. The U_{iso} for the H atoms were fixed at 1.3× the U_{iso} of the heavy atoms to which they are attached. The peak profiles were described using the generalized microstrain model (Stephens, 1999). The background was modeled using a six-term shifted Chebyshev polynomial, with a peak at 5.88° to model the scattering from the Kapton capillary and any amorphous component of the sample.

The final refinement (begun from the VASP-optimized structure described below) of 258 variables using 31,334 observations and 214 restraints yielded the residuals R_{wp} = 0.1673 and GOF = 3.14. The largest peak (1.59 Å from C58) and hole (1.92 Å from F3) in the difference Fourier map were 0.59(13) and − 0.54(13) eÅ^{-3}, respectively. The final Rietveld plot is shown in Figure 3. The largest features in the normalized error plot are in the intensities and shapes of low-angle peaks and an incomplete description of the background. A trace impurity may also be present.

The crystal structure of delamanid was optimized (fixed experimental unit cell) with density functional theory techniques using VASP (Kresse and Furthmüller, 1996) through the MedeA graphical interface (Materials Design, 2024). The calculation was carried out on 32 cores of a 144-core (768-GB memory) HPE Superdome Flex 280 Linux server at North Central College. The calculation used the GGA-PBE functional, a plane wave cutoff energy of 400.0 eV, and a *k*-point spacing of 0.2 Å^{-1}, leading to a 1 × 3 × 6 mesh, and took ~34.5 days. Single-point density functional calculations (fixed experimental cell) and population analysis were carried out using CRYSTAL23 (Erba et al., 2023). The basis sets for the H, C, N, and O atoms in the calculation were those of Gatti et al. (1994), and that for F was that of Peintinger et al. (2013). The calculations were run on a 3.5-GHz PC using eight *k*-points and the B3LYP functional, and took ~12.8 hours.

III. RESULTS AND DISCUSSION

The powder pattern of this study is similar enough to that reported by Duong et al. (2022) to suggest that they represent the same material (Figure 4), and thus our sample is representative of crystalline delamanid. A trace of a crystalline impurity may be present.

The root-mean-square (rms) Cartesian displacement of the non-H atoms in the Rietveld-refined and VASP-optimized structure of molecule 1(the lower atom numbers; Figure 5) is 0.833 Å, and the rms displacement for molecule 2 is 0.692 Å (Figure 6). These values are outside the normal range for correct structures (van de Streek and Neumann, 2014). The large number of variables, the relatively limited data range, and the pseudosymmetry conspire to make this a very difficult problem. The asymmetric unit is illustrated in Figure 7. Some of the U_{iso} refined to large values, suggesting the additional

https://doi.org/10.1017/S0885715625100845 Published online by Cambridge University Press

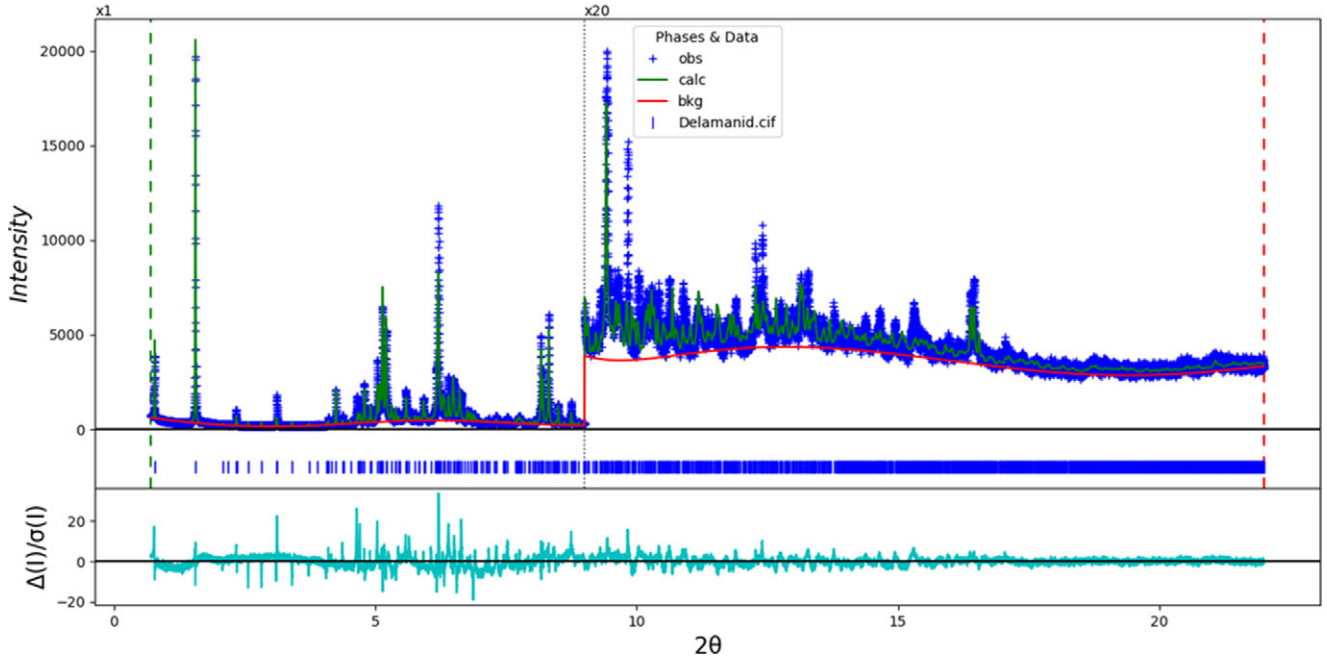

Figure 3. The Rietveld plot for delamanid. The blue crosses represent the observed data points, and the green line represents the calculated pattern. The cyan curve indicates the normalized error plot, and the red line indicates the background curve. The row of blue tick marks indicates the calculated delamanid reflection positions. The vertical scale has been multiplied by a factor of 20× for 2θ > 9.0°.

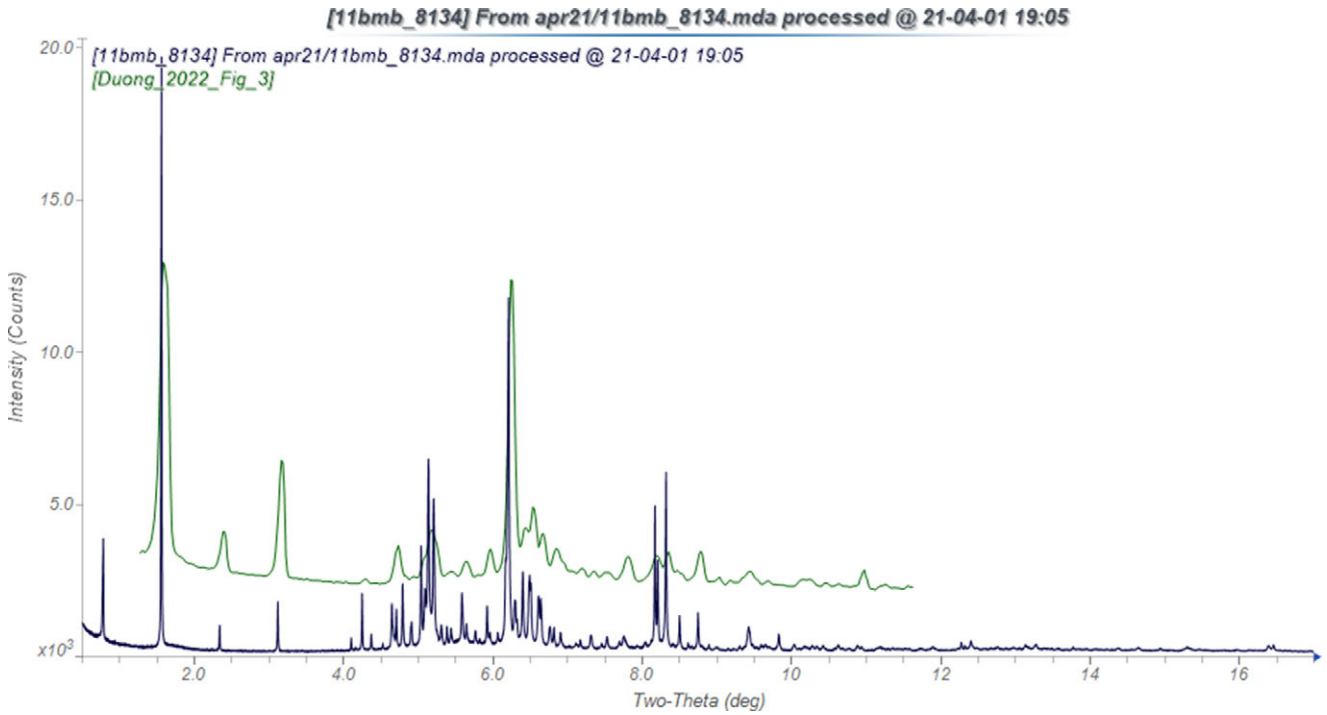

Figure 4. Comparison of the synchrotron pattern of delamanid (black) to that reported by Duong et al. (2022) (green). The literature pattern (measured using Cu K_α radiation) was digitized using UN-SCAN-IT (Silk Scientific, 2013) and converted to the synchrotron wavelength of 0.458133(2) Å using JADE Pro (MDI, 2024). Image generated using JADE Pro (MDI, 2024).

possibility of disorder. Since an ordered model is necessary for the density functional theory (DFT) optimization, we did not attempt to model disorder. The structure should be considered a proposed one, and we offer it in the hope that an improved model can be found. In the refined structure, there is a short intramolecular contact involving F41 of a trifluoromethyl group and the adjacent phenyl ring. This contact is relieved in the VASP-optimized structure. The remaining discussion will emphasize the VASP-optimized structure.

Most of the bond distances and bond angles fall within the normal ranges indicated by a Mercury Mogul Geometry check (Macrae et al., 2020). The C4–N24–C12 (140.6°; average = 135.6(12)°; *Z*-score = 4.1), C58–N49–C63 (141.1°; average = 135.6(12)°; *Z*-score = 4.5), and C65–C61–N48

https://doi.org/10.1017/S0885715625100845 Published online by Cambridge University Press

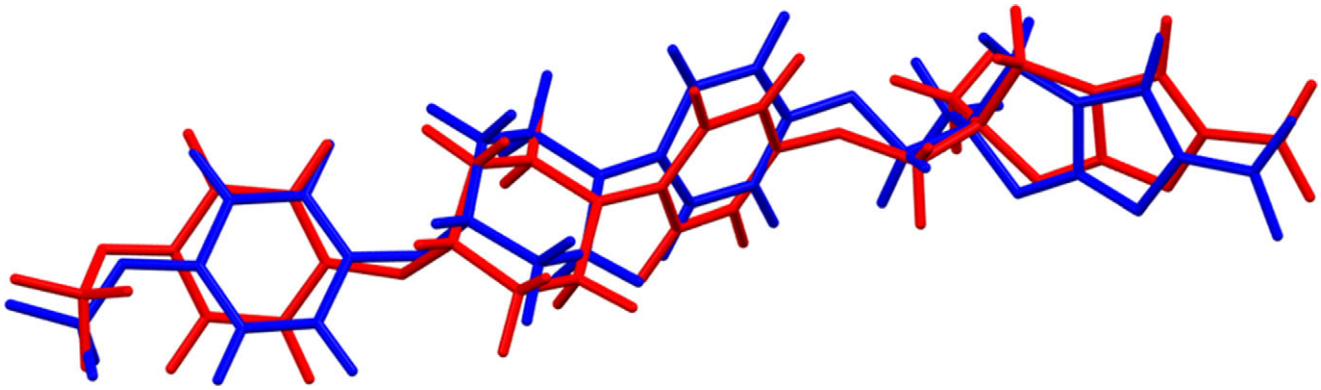

Figure 5. Comparison of the Rietveld-refined (red) and VASP-optimized (blue) structures of delamanid molecule 1. The root-mean-square Cartesian displacement is 0.833 Å. Image generated using Mercury (Macrae et al., 2020).

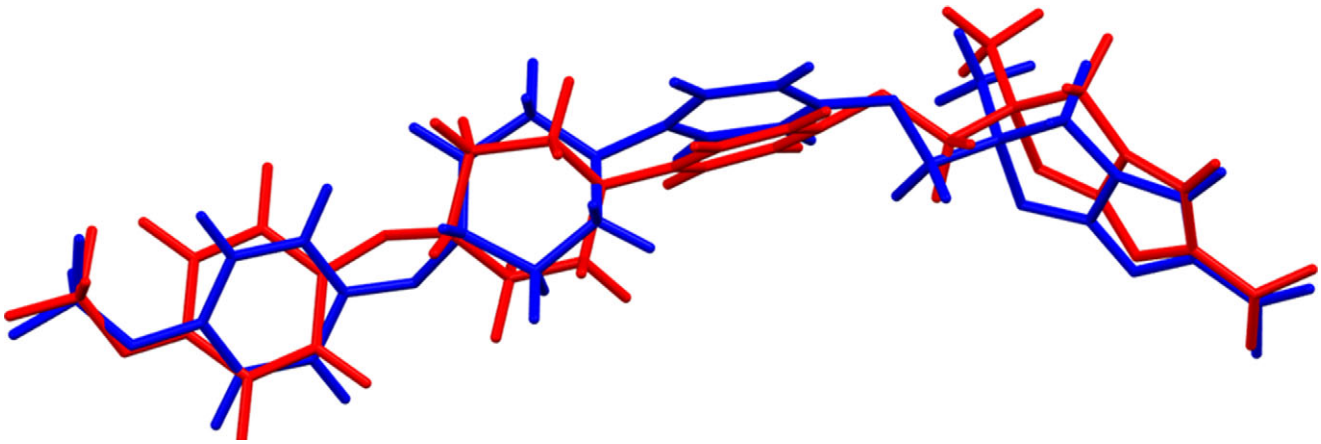

Figure 6. Comparison of the Rietveld-refined (red) and VASP-optimized (blue) structures of delamanid molecule 2. The root-mean-square Cartesian displacement is 0.692 Å. Image generated using Mercury (Macrae et al., 2020).

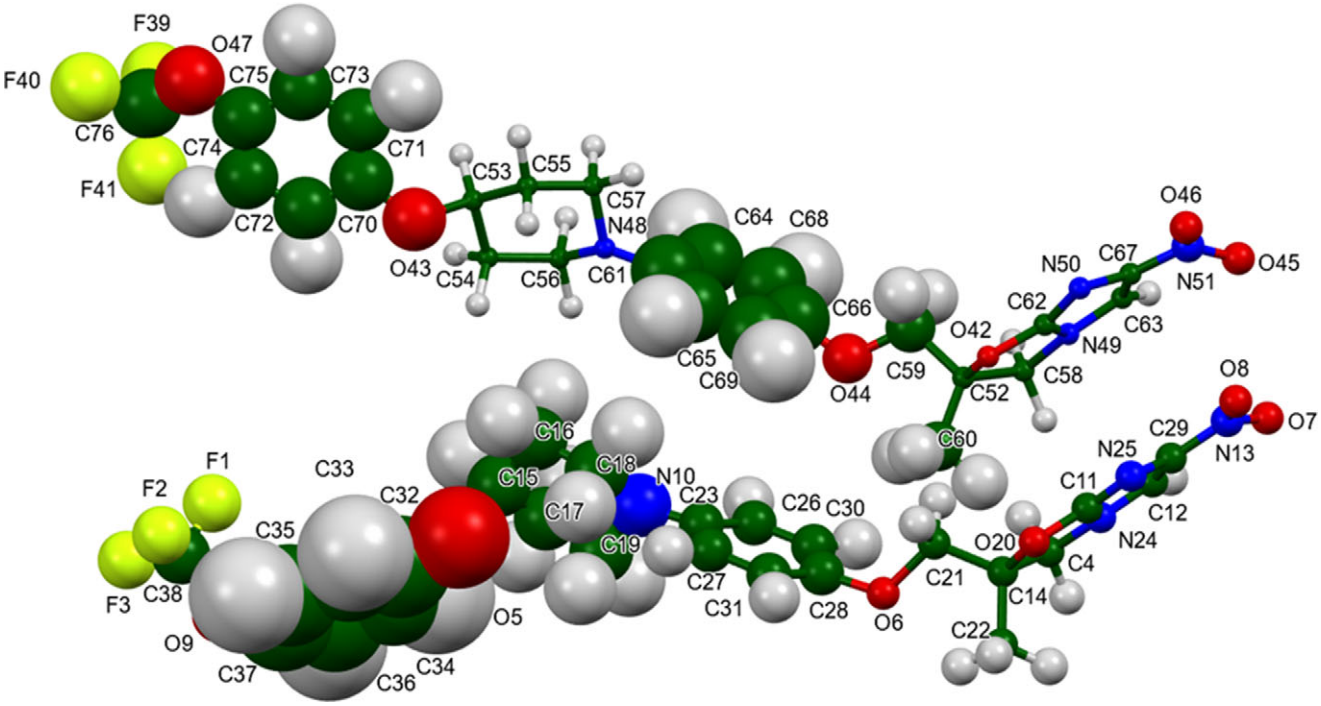

Figure 7. The asymmetric unit of delamanid, with the atom numbering. The atoms are represented by 50% probability spheroids. Image generated using Mercury (Macrae et al., 2020).

https://doi.org/10.1017/S0885715625100845 Published online by Cambridge University Press

(116.4°; average = 121.4(14)°; *Z*-score = 3.6) are flagged as unusual. The standard uncertainties on the averages are small, inflating the *Z*-scores. Torsion angles involving rotation about the O5–C32, O6–C28, O9–C37, C23–N10, O44–C59, O44–C66, O47–C75, C61–N48, and C59–C52 bonds are flagged as unusual. These lie on tails or in valleys of broad distributions, so the torsion angles are unusual but not unprecedented. The conformations of the molecules, especially around the ether oxygen atoms, are unusual.

There are two independent delamanid molecules, with different conformations (Figure 8). The rms Cartesian displacement is 1.085 Å. Quantum chemical geometry optimizations of the isolated molecules (DFT/B3LYP/6-31G*/water) using Spartan '24 (Wavefunction, 2023) indicated that they are essentially identical in energy ($\Delta E = 0.009$ kcal/mol). The global minimum-energy conformation is more similar to molecule 2 (rms displacement = 1.19 Å) but is only 0.1 kcal/mol lower in energy. The delamanid molecule is apparently very flexible, and intermolecular interactions determine the observed solid-state conformations.

The crystal structure (Figure 9) consists of layers of delamanid molecules perpendicular to the *a*-axis. The imidazooxazole

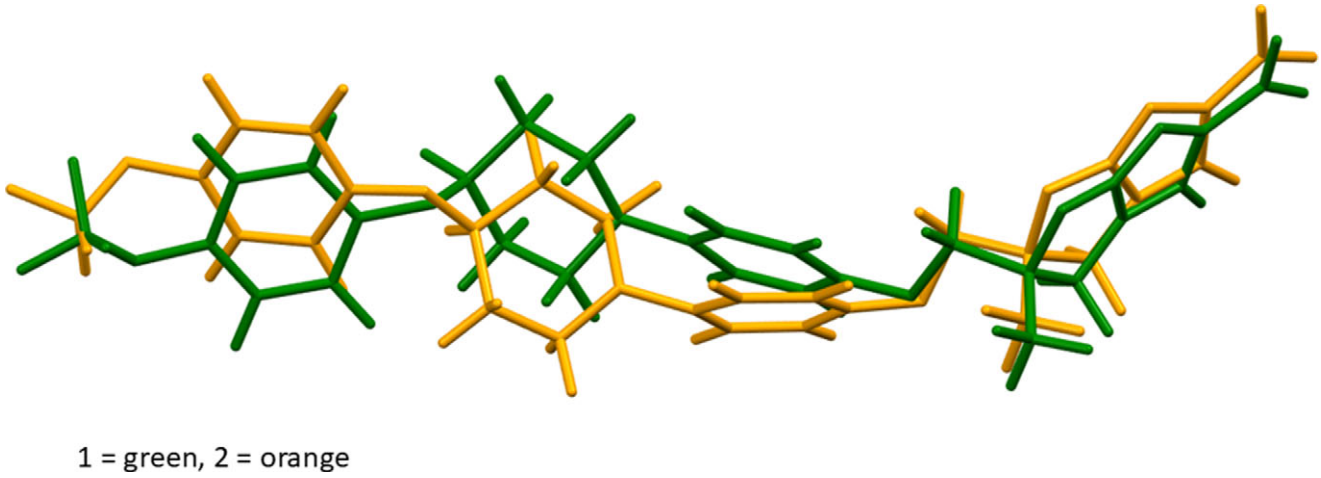

Figure 8. Comparison of DFT-optimized delamanid molecule 1 (green) and molecule 2 (orange). The root-mean-square Cartesian displacement is 1.085 Å.

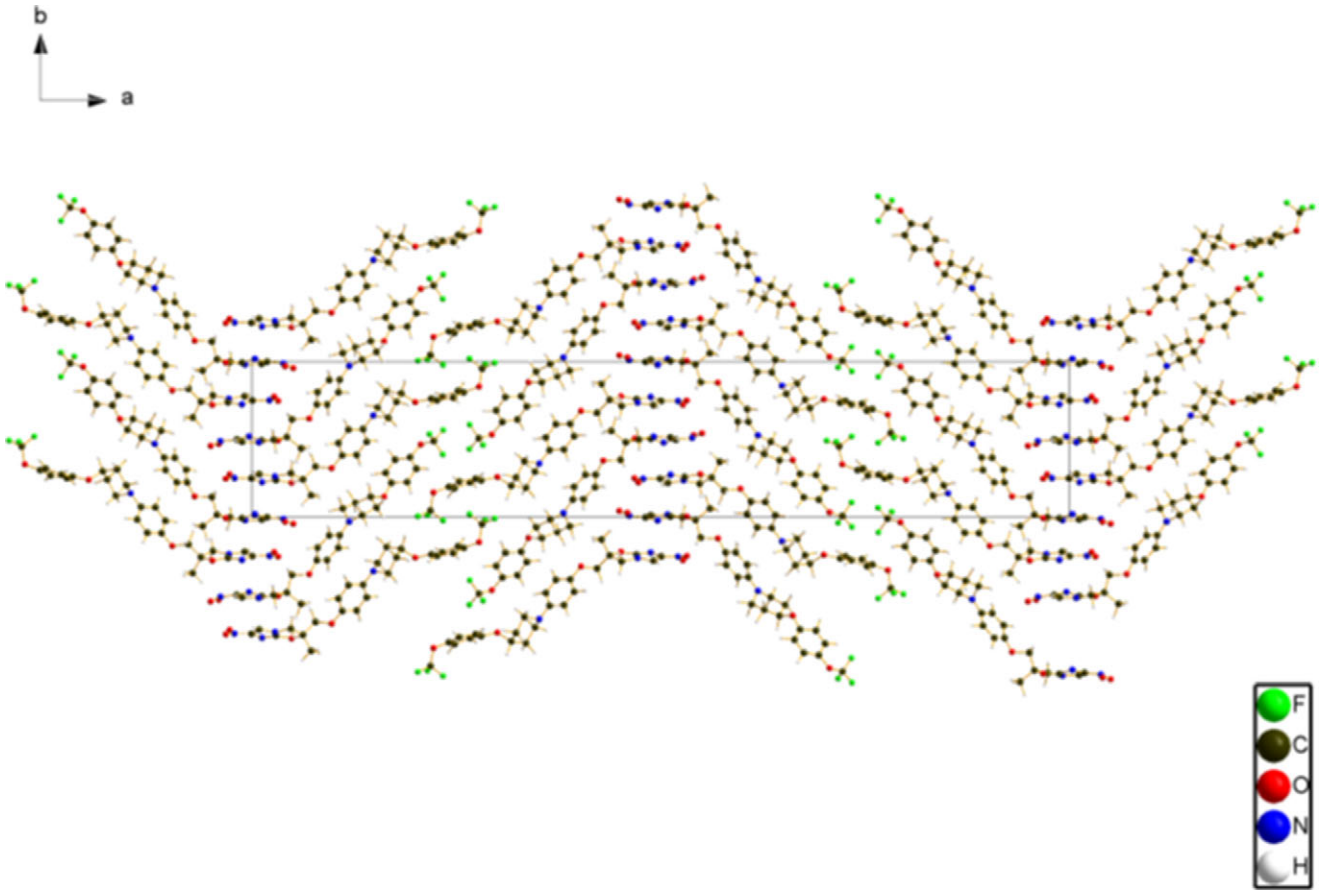

Figure 9. The crystal structure of delamanid, viewed down the *c*-axis. Image generated using Diamond (Crystal Impact, 2023).

https://doi.org/10.1017/S0885715625100845 Published online by Cambridge University Press

TABLE I. Hydrogen bonds (CRYSTAL23) in delamanid

H bond	D–H, Å	H···A, Å	D···A, Å	D–H···A, °	Overlap, *e*
C4–H78···O45	1.099	2.223	3.318	173.9	0.027
C12–H79···O8	1.087	2.227	3.300	168.7	0.029
C16–H82···N48	1.102	2.676	3.749	164.6	0.017
C55–H106···O6	1.096	2.323	3.375	160.3	0.018
C56–H108···O43	1.111	2.580	3.655	162.5	0.014
C58–H112···O7	1.098	2.292	3.382	171.5	0.022
C59–H114···O8	1.098	2.297	3.172	135.2	0.015
C60–H117···O44	1.097	2.461[a]	2.812	96.8	0.012
C63–H118···O46	1.088	2.314	3.381	166.4	0.027

[a]Intramolecular.

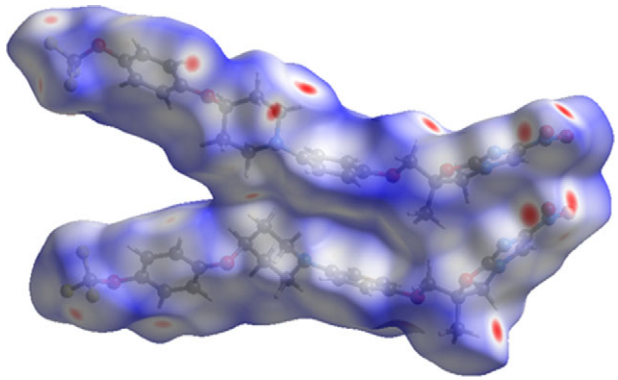

Figure 10. The Hirshfeld surface of delamanid. Intermolecular contacts longer than the sums of the van der Waals radii are colored blue, and contacts shorter than the sums of the radii are colored red. Contacts equal to the sums of radii are white. Image generated using CrystalExplorer (Spackman et al., 2021).

ring systems stack along the *b*-axis; the mean planes of the ring systems are approximately (1, 1, 0) and (−1, 1, 0). The trifluoromethyl groups make up the boundaries of the corrugated layers. The Mercury Aromatics Analyser indicates one moderate interaction with a distance of 4.50 Å, between the central phenyl ring of molecule 1 and the end ring of molecule 2, along with several weak interactions, with distances >5.79 Å. The shortest distances between the centroids of the imidazooxazole ring systems are 4.76 and 4.84 Å.

Analysis of the contributions to the total crystal energy of the structure using the Forcite module of Materials Studio (Dassault Systèmes, 2023) indicated that angle and torsion distortion terms dominate the intramolecular energy. The intermolecular energy is dominated by electrostatic attractions, which in this force-field-based analysis include hydrogen bonds. The hydrogen bonds are better discussed using the results of the DFT calculation.

There are no classical hydrogen bonds in the crystal structure (Table I). Eight C–H···O and one C–H···N hydrogen bonds contribute to the lattice energy. Molecule 2 acts as a donor in more hydrogen bonds than molecule 1.

The volume enclosed by the Hirshfeld surface of delamanid (Figure 10; Hirshfeld, 1977; Spackman et al., 2021) is 1,210.52 $Å^3$, 98.85% of the unit cell volume. The packing density is thus fairly typical. The volume/non-hydrogen atom is smaller than normal at 16.1 $Å^3$.

The Bravais–Friedel–Donnay–Harker (Bravais, 1866; Friedel, 1907; Donnay and Harker, 1937) algorithm suggests that we might expect platy morphology for delamanid (Figure 11), with {100} as the major faces, as expected from the extreme anisotropy of the lattice parameters. A sixth-order spherical harmonic model was included in the refinement. The texture index was 1.113(6), indicating that the preferred orientation was significant in this rotated capillary specimen.

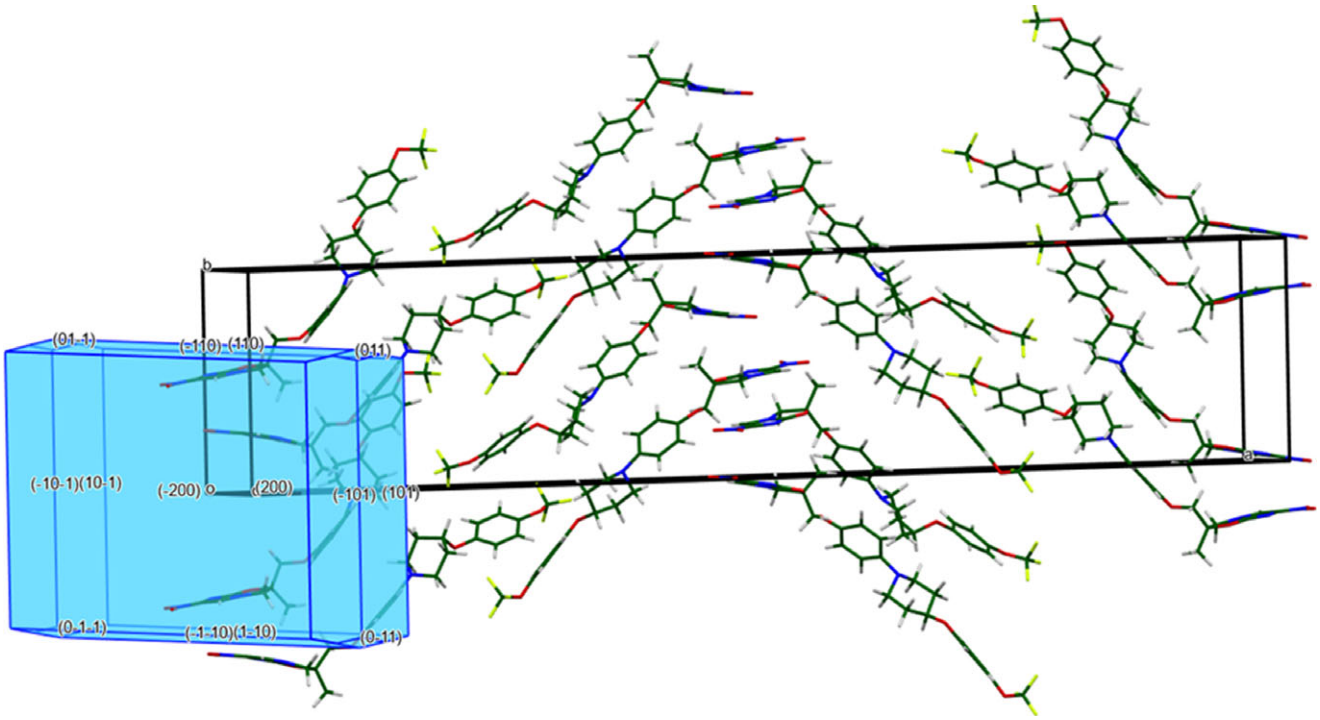

Figure 11. The predicted platy Bravais–Friedel–Donnay–Harker morphology of delamanid. Image generated using Mercury (Macrae et al., 2020).

https://doi.org/10.1017/S0885715625100845 Published online by Cambridge University Press

DEPOSITED DATA

The powder pattern of delamanid from a Le Bail fit of this synchrotron dataset has been submitted to the International Centre for Diffraction Data (ICDD) for inclusion in the Powder Diffraction File. The Crystallographic Information Framework (CIF) files containing the results of the Rietveld refinement (including the raw data) and the DFT geometry optimization were deposited with the ICDD. The data can be requested at pdj@icdd.com.

ACKNOWLEDGMENTS

We thank Saul Lapidus for his assistance in the data collection, and Christos Malliakas of Northwestern University and Jadupati Nag and Venkatraman Gopalan of The Pennsylvania State University for the measurement of the second-harmonic generation.

FUNDING STATEMENT

The use of the Advanced Photon Source at Argonne National Laboratory was supported by the U.S. Department of Energy, Office of Science, Office of Basic Energy Sciences, under Contract No. DE-AC02-06CH11357. This work was partially supported by the International Centre for Diffraction Data.

CONFLICTS OF INTEREST

The authors have no conflicts of interest to declare.

REFERENCES

Altomare, A., C. Cuocci, C. Giacovazzo, A. Moliterni, R. Rizzi, N. Corriero, and A. Falcicchio. 2013. "EXPO2013: A Kit of Tools for Phasing Crystal Structures from Powder Data." *Journal of Applied Crystallography* 46: 1231–35.

Antao, S. M., I. Hassan, J. Wang, P. L. Lee, and B. H. Toby. 2008. "State-of-the-Art High-Resolution Powder X-Ray Diffraction (HRPXRD) Illustrated with Rietveld Refinement of Quartz, Sodalite, Tremolite, and Meionite." *Canadian Mineralogist* 46: 1501–9.

Bravais, A. 1866. *Etudes Cristallographiques*. Gauthier Villars.

Bruno, I. J., J. C. Cole, M. Kessler, J. Luo, W. D. S. Motherwell, L. H. Purkis, B. R. Smith, et al. 2004. "Retrieval of Crystallographically Derived Molecular Geometry Information." *Journal of Chemical Information and Computer Sciences* 44: 2133–44.

Crystal Impact. 2023. *Diamond V. 5.0.0*. Crystal Impact – Dr. H. Putz & Dr. K. Brandenburg.

Dassault Systèmes. 2023. *BIOVIA Materials Studio 2024*. BIOVIA.

Donnay, J. D. H., and D. Harker. 1937. "A New Law of Crystal Morphology Extending the Law of Bravais." *American Mineralogist.* 22: 446–47.

Duong T. V., H. T. Nguyen, and L. S. Taylor. 2022. "Combining Enabling Formulation Strategies to Generate Supersaturated Solutions of Delamanid: *In Situ* Formation During Amorphous Solid Dispersion Fabrication for More Robust Release Profiles." *European Journal of Pharmaceutics and Biopharmaceutics* 174: 131–43.

Erba, A., J. K. Desmarais, S. Casassa, B. Civalleri, L. Donà, I. J. Bush, B. Searle, et al. 2023. "CRYSTAL23: A Program for Computational Solid State Physics and Chemistry." *Journal of Chemical Theory and Computation* 19: 6891–932. https://doi.org/10.1021/acs.jctc.2c00958.

European Medicines Agency, Committee for Medicinal Products for Human Use. 2013. Deltyba Assessment Report, Procedure No. EMEA/H/C/002552.

Friedel, G. 1907. "Etudes sur la loi de Bravais." *Bulletin de la Société Française de Minéralogie* 30: 326–455.

Gatti, C., V. R. Saunders, and C. Roetti. 1994. "Crystal-Field Effects on the Topological Properties of the Electron-Density in Molecular Crystals – the Case of Urea." *Journal of Chemical Physics* 101: 10686–96.

Gler, M. T., V. Skripconoka, E. Sanchez-Garavito, H. Xiao, J. L. Cabrera-Rivero, D. E. Vargas-Vasquez, M. Gao, et al. 2012. "Delamanid for Multidrug-Resistant Pulmonary Tuberculosis." *New England Journal of Medicine* 366: 2151–60.

Groom, C. R., I. J. Bruno, M. P. Lightfoot, and S. C. Ward. 2016. "The Cambridge Structural Database." *Acta Crystallographica Section B: Structural Science, Crystal Engineering and Materials* 72: 171–79.

Hirshfeld, F. L. 1977. "Bonded-Atom Fragments for Describing Molecular Charge Densities." *Theoretica Chemica Acta* 44: 129–38.

Kabekkodu, S., A. Dosen, and T. N. Blanton. 2024. "PDF-5+: A Comprehensive Powder Diffraction File™ for Materials Characterization." *Powder Diffraction* 39(2): 47–59.

Kaduk, J. A., C. E. Crowder, K. Zhong, T. G. Fawcett, and M. R. Suchomel. 2014. "Crystal Structure of Atomoxetine Hydrochloride (Strattera), $C_{17}H_{22}NOCl$." *Powder Diffraction* 29: 269–73.

Kim S., J. Chen, T. Cheng, A. Gindulyte, J. He, S. He, Q. Li, et al. 2023. "PubChem 2023 Update." *Nucleic Acids Research* 51 (D1): D1373–80. https://doi.org/10.1093/nar/gkac956.

Kresse, G., and J. Furthmüller. 1996. "Efficiency of Ab-Initio Total Energy Calculations for Metals and Semiconductors Using a Plane-Wave Basis Set." *Computational Materials Science* 6: 15–50.

Lardizabal, A. A., A. N. Khan, M. S. Bamrah, and N. D. Goswami. 2017. "Notes from the Field: Acquisition of Delamanid Under a Compassionate Use Program for Extensively Drug-Resistant Tuberculosis – United States." *Morbidity and Mortality Weekly Report* 67:996–97. https://doi.org/10.15585/mmwr.mm6735a6.

Lee, P. L., D. Shu, M. Ramanathan, C. Preissner, J. Wang, M. A. Beno, R. B. Von Dreele, et al. 2008. "A Twelve-Analyzer Detector System for High-Resolution Powder Diffraction." *Journal of Synchrotron Radiation* 15: 427–32.

Louër, D., and A. Boultif. 2014. "Some Further Considerations in Powder Diffraction Pattern Indexing with the Dichotomy Method." *Powder Diffraction* 29: S7–S12.

Macrae, C. F., I. Sovago, S. J. Cottrell, P. T. A. Galek, P. McCabe, E. Pidcock, M. Platings, et al. 2020. "*Mercury 4.0*: From Visualization to Design and Prediction." *Journal of Applied Crystallography* 53: 226–35.

Materials Design. 2024. *MedeA 3.7.2*. Materials Design, Inc.

MDI. 2024. *JADE Pro Version 9.0*. Materials Data.

Mudde, S. E., A. M. Upton, A. Lenaerts, H. I. Bax, and J. E. M. De Steenwinkel. 2022. "Delamanid or Pretomanid? A Solomonic Judgement!" *Journal of Antimicrobial Chemotherapy* 77: 880–902.

Peintinger, M. F., D. Vilela Oliveira, and T. Bredow. 2013. "Consistent Gaussian Basis Sets of Triple-Zeta Valence with Polarization Quality for Solid-State Calculations." *Journal of Computational Chemistry* 34: 451–59.

Pontali, E., R. Centis, L. D'Ambrosio, F. Toscanini, and G. B. Migliori. 2019. "Recent Evidence on Delamanid Use for Rifampicin-Resistant Tuberculosis." *Journal of Thoracic Disease* 11: S457–60.

Silk Scientific. 2013. *UN-SCAN-IT 7.0*. Silk Scientific Corporation.

Spackman, P. R., M. J. Turner, J. J. McKinnon, S. K. Wolff, D. J. Grimwood, D. Jayatilaka, and M. A. Spackman. 2021. "CrystalExplorer: A Program for Hirshfeld Surface Analysis, Visualization and Quantitative Analysis of Molecular Crystals." *Journal of Applied Crystallography* 54: 1006–11. https://doi.org/10.1107/S1600576721002910; https://crystalexplorer.scb.uwa.edu.au.

Stephens, P. W. 1999. "Phenomenological Model of Anisotropic Peak Broadening in Powder Diffraction." *Journal of Applied Crystallography* 32: 281–89.

Sykes, R. A., P. McCabe, F. H. Allen, G. M. Battle, I. J. Bruno, and P. A. Wood. 2011. "New Software for Statistical Analysis of Cambridge Structural Database Data." *Journal of Applied Crystallography* 44: 882–86.

Toby, B. H., and R. B. Von Dreele. 2013. "GSAS II: The Genesis of a Modern Open Source All Purpose Crystallography Software Package." *Journal of Applied Crystallography* 46: 544–49.

van de Streek, J., and M. A. Neumann. 2014. "Validation of Molecular Crystal Structures from Powder Diffraction Data with Dispersion-

https://doi.org/10.1017/S0885715625100845 Published online by Cambridge University Press

Corrected Density Functional Theory (DFT-D)." *Acta Crystallographica Section B: Structural Science, Crystal Engineering and Materials* 70: 1020–32.

Wang, J., B. H. Toby, P. L. Lee, L. Ribaud, S. M. Antao, C. Kurtz, M. Ramanathan, R. B. Von Dreele, and M. A. Beno. 2008. "A Dedicated Powder Diffraction Beamline at the Advanced Photon Source: Commissioning and Early Operational Results." *Review of Scientific Instruments* 79: 085105. https://doi.org/10.1063/1.2969260.

Wavefunction, Inc. 2023. *Spartan '24. V. 1.0.0*. Wavefunction, Inc.

Xavier, A. S., and M. Lakshmanan. 2014. "Delamanid: A New Armor in Combating Drug-Resistant Tuberculosis." *Journal of Pharmacology and Pharmacotherapeutics* 5: 222–24.

Zhao, J., S. Siddiqui, S. Shang, Y. Bian, S. Bagchi, Y. He, and C.-R. Wang. 2015. "Mycolic Acid-Specific T Cells Protect Against Mycobacterium Tuberculosis Infection in a Humanized Transgenic Mouse Model." *eLife* 4: e08525. https://doi.org/10.7554/eLife.08525.

https://doi.org/10.1017/S0885715625100845 Published online by Cambridge University Press